PAPER

Check for updates

Ambipolar charge-trapping in self-assembled nanostructures of a supramolecular miktoarm star-shaped copolymer with a zinc phthalocyanine core†

Xinhao Zhong,[ab] Debdatta Panigrahi, [iD][c] Ryoma Hayakawa, [iD][c] Yutaka Wakayama, [iD]*[c] Koji Harano, [iD][d] Masayuki Takeuchi [iD]*[ab] and Junko Aimi [iD]*[a]

Nonvolatile organic field-effect transistor (OFET) memories have attracted considerable attention owing to their potential applications in flexible and wearable electronic devices. The novel design of a charge-trapping material based on supramolecular miktoarm star copolymers (μ-stars) consisting of star-shaped polystyrene with a zinc phthalocyanine core (ZnPcPS$_4$) and a pyridyl end-functionalized polymer (py-polymer) has been studied to explore the influence of self-assembled morphology on the final device performances. Supramolecular μ-stars containing the ZnPc core showed distinctive phase-separated nanostructures in the films that were different from typical polymer blends. The OFET memory devices embedded with supramolecular μ-stars exhibited ambipolar charge-trapping behavior with photoresponsive characteristics, resulting in a wide memory window (47 V) with a high on/off current ratio ($>10^7$) for a long period of time ($>10^4$ s). Furthermore, the charge-trapping properties of the polymer memory layer were studied using Kelvin probe force microscopy (KPFM), revealing enhanced charge-trapping capabilities attributed to nanoscale phase separation in the supramolecular μ-stars. This study provides the design and concept of charge-trapping materials for next-generation high-performance OFET memory devices.

Introduction

Nonvolatile organic field-effect transistor (OFET) memory devices, designed to retain data post-power disruption, hold significant promise for integration into flexible and wearable organic electronic devices, such as cost-effective wireless tags and biosensors.[1–3] OFET memory involves an architecture wherein a memory layer is inserted between the charge-transporting layer and the gate electrodes. Various materials, including ferroelectric materials,[4–6] polymer electrets,[7,8] and

nano-floating gates,[9–11] have been employed as memory layers in OFET devices. Memory characteristics originate from field-effect modulation by spontaneous polarization in ferroelectrics or charge trapping in dielectrics.[12,13] To introduce these memory layers into OFETs while maintaining transistor performance, polymer-based memory materials offer advantages in terms of ease of fabrication and application to flexible devices.

The memory performance of the device is assessed based on the memory window, which denotes the shift in the threshold voltage (ΔV_{th}) caused by trapped charges or polarized dipoles within the memory material. A large memory window facilitates easier differentiation between the "0" and "1" digital states at the reading voltage. Additionally, controllable memory shifts are advantageous for achieving multilevel data storage, thus further enhancing the memory capacity without enlarging the device size.[14,15] The magnitude of the memory window is influenced by the density of charge-trapping sites and the intensity of the applied electric field in the tunneling layer, potentially affecting the retention ability due to charge leakage from insufficient insulation of the adjacent charge-trapping sites.[16] Extensive research has demonstrated that morphological control of the charge-trapping layer is crucial for optimizing

[a] Research Center for Macromolecules and Biomaterials, National Institute for Materials Science (NIMS), 1-2-1 Sengen, Tsukuba, Ibaraki 305-0047, Japan. E-mail: AIMI.Junko@nims.go.jp, TAKEUCHI.Masayuki@nims.go.jp

[b] Department of Materials Science and Engineering, Faculty of Pure & Applied Sciences, University of Tsukuba, 1-1-1 Tennodai, Tsukuba, Ibaraki 305-8577, Japan

[c] Research Center for Materials Nanoarchitectonics (MANA), NIMS, 1-1 Namiki, Tsukuba, Ibaraki 305-0044, Japan. E-mail: WAKAYAMA.Yutaka@nims.go.jp

[d] Center for Basic Research on Materials, NIMS, 1-1 Namiki, Tsukuba, Ibaraki 305-0044, Japan

† Electronic supplementary information (ESI) available. See DOI: https://doi.org/10.1039/d4tc01265h

9642 | *J. Mater. Chem. C*, 2024, **12**, 9642–9651

This journal is © The Royal Society of Chemistry 2024

the memory performance.[12,16–18] Notably, microstructures formed by the self-assembly of block copolymers have been studied for preparing well-defined charge-trapping layers.[19–22] For instance, Leong *et al.* demonstrated *in situ* synthesis of Au nanoparticles within self-assembled poly(styrene-*b*-poly(4-vinyl pyridine)) block copolymers to prepare well-defined nano-floating gates. The phase morphology of the block copolymer affected the loading density of the nanoparticles, thereby controlling the memory window.[23] Chiu *et al.* reported OFET memory utilizing sugar-based block copolymers containing maltoheptaose (MH), where the orientation of microdomains influenced the memory window.[24] Ambipolar charge-trapping was also achieved by introducing 1-aminopyrene into the polymer microdomains *via* supramolecular interactions. Yang *et al.* recently introduced a pyrene-functionalized block copolymer for photoresponsive memory.[25] Phototransistor memory, which operates *via* light irradiation rather than voltage application, has been gaining importance because of its low energy consumption and rapid data processing.[26–30] Phototransistor memory has recently been applied to artificial synaptic memory that mimics the human brain.[31] This uses optical signals to mimic the synapses responsible for information transmission between nerve cells, where memory depends on the intensity or frequency of external stimuli. Such integration of nonvolatile data storage and processing functions into a single OFET device has potential applications for neuromorphic devices which are attracting attention in the field of artificial intelligence and deep learning.[32,33]

We recently developed OFET memory devices using a star-shaped polymer with a metallophthalocyanine (MPc) core as a nano-floating gate (Fig. 1(a)).[34–36] The MPc core acts as a charge-trapping site, whereas the surrounding polymer arms hinder charge leakage to achieve nonvolatile characteristics. Taking advantage of polymer-based nano-floating gates, the MPc-cored star polymer was easily fabricated into logic circuits such as inverters, demonstrating multilevel or reconfigurable logic-in-memory applications.[37,38] In this polymer nano-floating gate system, the memory window of the OFET memory has been expanded by increasing the density of the MPc core in the polymer film, which was controlled by the length of the polymer arms using precision polymer synthesis.[35] On the

other hand, increasing the core density shortened the memory retention time and decreased the charge carrier mobility of the organic semiconductor. The shorter retention time was attributed to potential charge leakage arising from insufficient insulation of the adjacent MPc core charge-trapping sites. The decrease in the charge carrier mobility was linked to the crystal growth of the organic semiconductor, which was influenced by the structure of the polymer thin film. The phase morphology of the memory material appears to be critical to the memory performance, particularly the memory window and charge retention properties.

In this study, an OFET memory with ambipolar charge-trapping characteristics is demonstrated. Supramolecular miktoarm star copolymers (μ-stars) composed of star-shaped polystyrene with a zinc phthalocyanine core (ZnPcPS$_4$) and pyridyl end-functionalized polymers (py-polymer) as memory materials (Fig. 1(b)) have been utilized.[39] Asymmetric polymers, such as block copolymers and miktoarm star copolymers, are known to show unique phase behavior *via* self-assembly.[40–42] By using metal–ligand coordination, AB$_4$-type supramolecular μ-stars with a functional core were facilely prepared without a tedious synthetic procedure (Fig. 1(c)). We expect that the morphology of the asymmetric star-shaped polymers may influence the device performance in OFET memory. The thin-film morphology and charge-trapping behavior of supramolecular μ-stars were investigated by atomic force microscopy (AFM), transmission electron microscopy (TEM), and Kelvin probe force microscopy (KPFM). The polymer films containing supramolecular μ-stars showed a unique morphology characteristic of microphase separation, which is different from normal blend polymers. Polymer films containing the ZnPc core were further fabricated for OFET memory, showing ambipolar charge-trapping behavior by electronic and photo-assisted programming/erasing operations. This OFET memory possessed long memory retention capability, which was further enhanced by the microphase separation of μ-stars. The relationship between the phase morphology and charge-trapping behavior was investigated.

Experimental section

Materials

Commercial chemicals purchased from Aldrich Chemical Co., Inc., TCI, Wako Chemicals, FUJIFILM Wako Pure Chemical Corporation, and Kanto Chemicals were used without further purification, unless noted otherwise.

Measurements

Atomic force microscopy (AFM) was performed under ambient conditions using Bruker Dimension Icon and Dimension IconIR. Surface morphology imaging was conducted in the ScanAsyst mode using a silicon cantilever (ScanAsyst-Air). Nanoscale infrared (IR) spectroscopy was conducted in the IIR tapping mode using a gold-coated silicon cantilever (PR-UM-TNIR-D-10). X-ray diffraction (XRD) measurements were
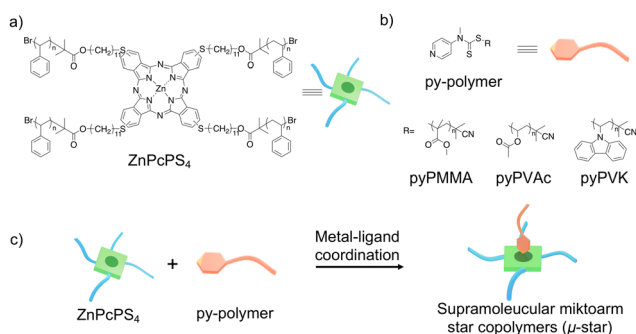

Fig. 1 Chemical structures of ZnPcPS$_4$ (a) and py-polymers (b). (c) Preparation of a supramolecular miktoarm star-shaped copolymer with a ZnPc core through coordination interaction.

This journal is © The Royal Society of Chemistry 2024

J. Mater. Chem. C, 2024, **12**, 9642–9651 | 9643

performed using a Bruker D8 Discover with a Cu Kα X-ray source. Transmission electron microscopy (TEM), high-angle annular dark-field (HAADF) scanning transmission electron microscopy (STEM), and energy-dispersive spectroscopy (EDS) analyses were conducted using a Thermo Fisher Scientific Talos F200X G2 equipped with an EDS detector (Super-X G2) at an acceleration voltage of 80 kV. The specimens were prepared by scooping a thin film of polymer in water using a TEM copper grid with a lacy carbon support (NS-C15, Okenshoji Co., Ltd). The probe current for HAADF-STEM microscopy and EDS mapping was set to 1.6 nA. EDS analysis was xperformed using Velox software (Thermo Fisher Scientific) with a single three-parameter Bethe-Heitler function as the background correction parameter. Kelvin probe force microscopy (KPFM) measurements were completed using a scanning probe microscope (Shimadzu, SPM-9700HT) under ambient conditions. A conductive silicon tip coated with a Pt–Ir alloy was used as the cantilever (Nanoworld, EFM). The voltage applied to the cantilever was controlled by using a source measurement unit (Keysight Technology, B2912A).

Device fabrication and measurement

OFET memory devices with a C8-BTBT organic semiconductor layer were prepared on a highly doped p$^+$-Si (001) substrate with a 200 nm thick SiO$_2$ layer. First, the substrates were cleaned *via* sequential ultrasonication in acetone and ethanol. Subsequently, a thin layer of the polymer was spin-coated onto the SiO$_2$ surface. The organic semiconductor C8-BTBT was vacuum-deposited onto the polymer film using shadow masks. The top-contact gold electrodes were thermally deposited as the source and drain electrodes using another shadow mask to complete the transistor fabrication process. Light-assisted memory operations were performed using a xenon lamp (Asahi Spectra, MAX-303) with ultraviolet (UV) light (250–380 nm) and LED lamps (730 and 365 nm, Asahi Spectra, CL-1501).

Electrical measurements were performed using an Agilent B1500A semiconductor parameter analyzer under ambient conditions. The charge carrier mobility (μ) and threshold voltage (V_{th}) values were estimated from the slope and intercept of the linear plot of the square root of the drain-to-source current ($I_{ds}^{1/2}$) *vs.* the gate voltage (V_g) in the saturation regime using the following equation:

$$I_{ds} = WC_{tot}\mu\frac{(V_g - V_{th})^2}{2L} \qquad (1)$$

where C_{tot} is the capacitance per unit area of the total dielectric layer and L and W are the channel length and width, respectively.

The relationships between the capacitances of the device (C_{tot}), SiO$_2$ wafer (C_{SiO_2}), and polymers (C_{poly}) and the polymer dielectric constant (ε) are defined as follows:

$$\frac{1}{C_{tot}} = \frac{1}{C_{poly}} + \frac{1}{C_{SiO_2}} \qquad (2)$$

$$C_{poly} = \frac{\varepsilon_0\varepsilon}{d} \qquad (3)$$

where ε_0 is the vacuum permittivity (8.854×10^{-12} F m^{-1}), d is the thickness of the dielectric, and C_{SiO_2} is 17.7 nF cm^{-2}. The total capacitances (C_{tot}) were calculated using the estimated dielectric constants of 2.88, 2.35, and 4.66 for ZnPcPS$_4$/pyPMMA, ZnPcPS$_4$, and pyPMMA, respectively.

Results and discussion

Morphology of a supramolecular miktoarm star copolymer

The supramolecular μ-stars were formed by blending ZnPcPS$_4$ and pyridine-tethered polymers (py-polymer) in organic solvents. In the previous study, we prepared three types of py-polymers, poly(methyl methacrylate) (pyPMMA), poly(vinyl acetate) (pyPVAc), and poly(*N*-vinyl carbazole) (pyPVK), by reversible addition–fragmentation chain transfer (RAFT) polymerization (Fig. 1(b)).[39] The average molecular weights (M_n) of each py-polymer were 13.9 kg mol^{-1} for pyPMMA, 16.1 kg mol^{-1} for pyPVAc, and 13.0 kg mol^{-1} for pyPVK, respectively. They have similar M_n to that of ZnPcPS$_4$ (14.2 kg mol^{-1}) (Table S1, ESI†). The metal–ligand coordination between ZnPcPS$_4$ and three types of py-polymers in solution has been confirmed by spectral studies by means of UV-vis absorption and ^{1}H-NMR measurements.[39] To investigate the phase morphologies of polymer films containing supramolecular μ-stars, polymer films were prepared by spin-coating each polymer mixture (5 mg mL^{-1}) in a mass ratio of 1:1. Notably, the M_n of the py-tethered polymers was similar to that of ZnPcPS$_4$, which is considered to have a molar ratio of approximately 1:1, corresponding to the 1:1 complexation observed between the ZnPc core and the pyridyl end-group. Another set of polymer films containing py-polymers and star-shaped polystyrene without a ZnPc core (PS$_4$) was prepared. The M_n of PS$_4$ is 16 kg mol^{-1}, which is similar to that of ZnPcPS$_4$. Binary polymer blends of PS/PMMA, PS/PVAc, and PS/PVK are known to exhibit various phase-separated structures due to the strong segregation between immiscible polymers.[43,44] Therefore, the differences in film morphology with and without the ZnPc core were investigated to ascertain the influence of the supramolecular interactions on the polymer blend.

The surface morphologies of the polymer blend films were analyzed by AFM. Fig. 2(a) shows the AFM height image of a film spin-coated from a toluene solution of a mixture of ZnPcPS$_4$ and pyPMMA (ZnPcPS$_4$/pyPMMA). The film exhibited a distinct phase separation with a domain size of approximately
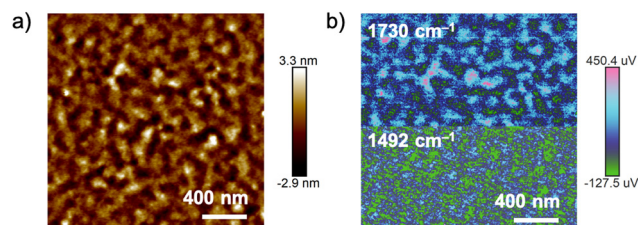

Fig. 2 (a) AFM height image of a blended film of ZnPcPS$_4$/pyPMMA. (b) AFM-IR image of a blended film of ZnPcPS$_4$/pyPMMA by monitoring at 1730 cm^{-1} (top) and 1492 cm^{-1} (bottom).

9644 | *J. Mater. Chem. C*, 2024, **12**, 9642–9651

This journal is © The Royal Society of Chemistry 2024

50 nm. The phase-separated morphology was analyzed using AFM combined with nanoscale infrared (IR) spectroscopy (AFM-IR). The AFM image was monitored at selected absorption wavenumbers of 1730 and 1492 cm^{-1}, corresponding to the carbonyl stretching band of PMMA and the benzene C=C stretching vibrations of PS, respectively. As shown in Fig. 2(b), the relatively higher and brighter parts in the AFM image were characterized as the PMMA domain, whereas the other domains were dominated by PS. In contrast, the blend polymer film containing PS$_4$ and pyPMMA exhibited irregular and micrometer-sized phase separation in the AFM height image (Fig. S1, ESI†). The root-mean-square (RMS) surface roughness (Rq) of the blended polymer film of PS$_4$ and pyPMMA was estimated to be 1.36 nm, which was larger than that of the ZnPcPS$_4$/pyPMMA film (0.49 nm). The smoother film surfaces and smaller domain sizes of phase separation implied the influence of coordination interaction between ZnPc and the pyridyl end-group in the supramolecular μ-star.

The film morphology of the supramolecular μ-star was further investigated by TEM. A 1 wt% toluene solution of ZnPcPS$_4$/pyPMMA was dropped onto the water surface to form a thin film and a portion of the film was scooped onto a TEM grid with a carbon support layer. A contrast between the phase-separated PS and PMMA domains was observed in the bright-field TEM images of the unstained samples (Fig. S2, ESI†). Fig. 3(a) shows a HAADF-STEM image of the supramolecular μ-star film, exhibiting clear phase-separated images with a domain size of 20–50 nm. Elemental mapping of the film using STEM-EDS revealed that the brighter regions of the HAADF-STEM image had a higher carbon content than the darker regions, whereas the darker regions overlapped with oxygen-rich domains (Fig. 3(b)). This result indicates that the bright region corresponds to the PS domain, whereas the other domain is dominated by PMMA. Notably, the elemental mapping of Zn in ZnPcPS$_4$ overlapped with the carbon-rich domains and showed a bright contrast in the HAADF-STEM image owing to the presence of heavy atoms (Fig. S3, ESI†). The film morphology observed by TEM was similar to that observed in the aforementioned AFM images, confirming that the ZnPcPS$_4$/pyPMMA films exhibited phase-separated nanodomains. The coordination interaction between the ZnPc core in ZnPcPS$_4$ and the pyridyl end group of pyPMMA might connect the boundaries between incompatible polymers, reducing the interfacial tension to exhibit microphase separation like that of block copolymers rather than macrophase separation, which is often observed in normal polymer blends. In other words, the supramolecular complexes (μ-stars) in the polymer blend act as a compatibilizer, providing nanosized phase-separated morphology and reducing surface roughness.

Similarly, the surface morphologies of other supramolecular μ-stars (ZnPcPS$_4$/pyPVAc and ZnPcPS$_4$/pyPVK blends) spin-coated from dichloromethane solution were also analyzed by AFM (Fig. 4). A polymer film containing ZnPcPS$_4$ and pyPVAc exhibited distinct phase separation (Fig. 4(a)), whereas the film from a mixture of PS$_4$ and pyPVAc displayed a droplet-like morphology owing to the strong phase segregation between PVAc and PS (Fig. 4(c)). The surface roughness Rq of ZnPcPS$_4$/pyPVAc was 6.28 nm, and it was much smoother than the PS$_4$/pyPVAc blended film (30.4 nm). A similar trend was observed for the blended films containing PS and PVK. The polymer containing ZnPcPS$_4$/pyPVK showed nanoscale phase separation (Fig. 4(b)), whereas stronger phase segregation and a relatively rough surface were observed in the PS$_4$/PVK blended film (Fig. 4(d)). These results support the abovementioned assumption that metal–ligand coordination between the ZnPc core and pyridyl end-groups in the polymers influences the bulk film morphology of the blended polymers. Such nanostructures from microphase separation are often observed in block copolymers or μ-stars; however, the preparation of various asymmetric polymers is normally difficult due to tedious synthetic procedures. In this study, phase-separated nanostructures of polymer films composed of various polymer blend combinations were successfully obtained by exploiting supramolecular interactions.

Characteristics of OFET memory using the supramolecular μ-star

The unique phase-separated morphology of the supramolecular μ-star with the ZnPc core was then utilized in the memory layer of an OFET memory device. To develop the OFET memory, a ZnPcPS$_4$/pyPMMA film was chosen that formed a relatively flat surface, allowing ideal crystal growth of the organic
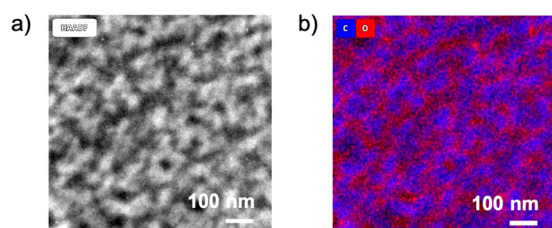

Fig. 3 (a) HAADF–STEM image and (b) EDS elemental mapping image of carbon (blue) and oxygen (red) for the ZnPcPS$_4$/pyPMMA film.
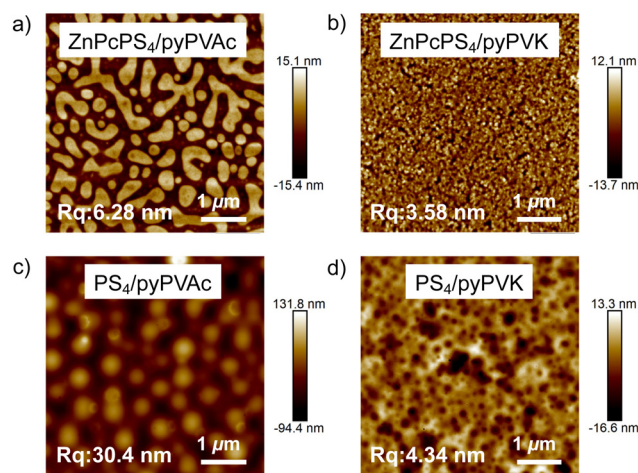

Fig. 4 AFM height images of blended films of (a) ZnPcPS$_4$/pyPVAc, (b) ZnPcPS$_4$/pyPVK, (c) PS$_4$/pyPVAc, and (d) PS$_4$/pyPVK.

This journal is © The Royal Society of Chemistry 2024

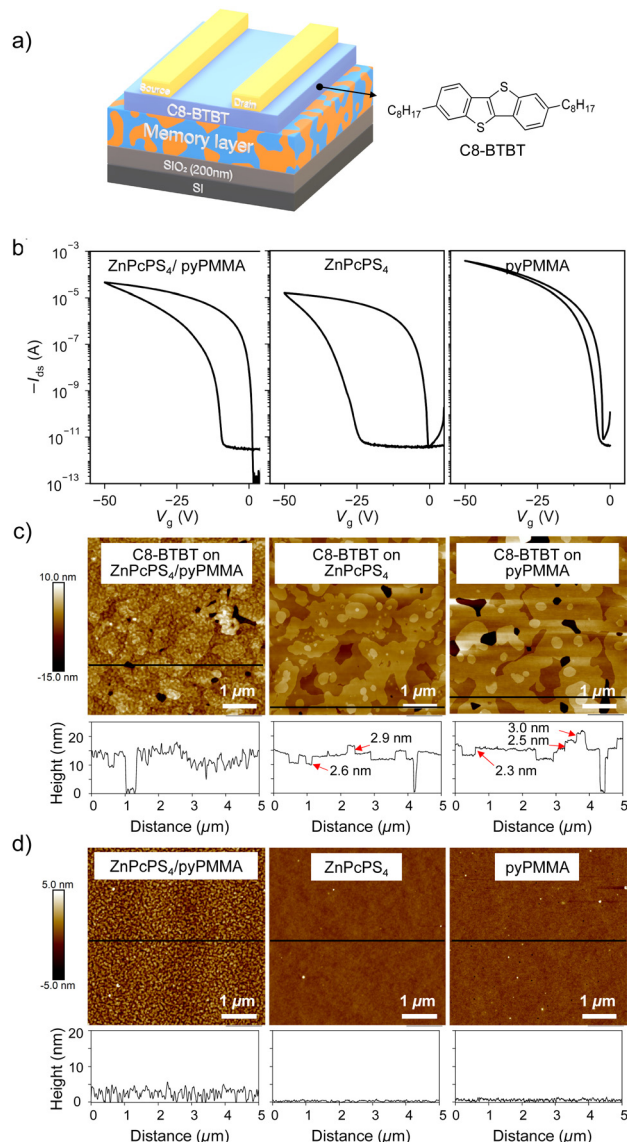*J. Mater. Chem. C*, 2024, **12**, 9642–9651 | **9645**

Fig. 5 (a) Device architecture of C8-BTBT-based OFET memory with a polymer memory layer. (b) Transfer characteristics of OFET memory devices with memory layers of ZnPcPS$_4$/pyPMMA (left), ZnPcPS$_4$ (middle), and pyPMMA (right). AFM height images and cross-sectional profiles of (c) C8-BTBT and (d) polymer layers.

semiconductor. A 2 wt% toluene solution of ZnPcPS$_4$/pyPMMA in a 1:1 mass ratio was spin-coated on a Si wafer with 200 nm SiO$_2$, followed by vacuum deposition of 2,7-dioctyl[1]benzo-thieno[3,2-b][1]benzothiophene (C8-BTBT)[45] and gold electrodes. The device architecture with a bottom-gate top-contact configuration is shown in Fig. 5(a). The thicknesses of the memory layer and the C8-BTBT layer estimated by X-ray reflectivity measurements were 27.0 and 14.9 nm, respectively. OFET memory devices embedded with ZnPcPS$_4$ or pyPMMA memory layers were also prepared for comparison.

The transfer and output characteristics of the fabricated OFET devices are shown in Fig. 5(b) and Fig. S4 (ESI†), respectively. A typical p-type accumulation mode with sweep

direction dependence was observed for the fabricated OFET devices. The estimated charge carrier mobility (μ), on/off current ratio (I_{on}/I_{off}), and initial threshold voltage (V_{th}) are listed in Table S2 (ESI†). The charge carrier mobility of the OFET with the ZnPcPS$_4$/pyPMMA layer was estimated to be 0.43 cm^2 V^{-1} s^{-1}, which is slightly higher than that of the ZnPcPS$_4$-embedded device of 0.33 cm^2 V^{-1} s^{-1}. This result indicated that the phase-separated morphology of the under-lying supramolecular µ-star did not disturb the charge trans-port properties in the C8-BTBT semiconductor layer. However, the morphology of the C8-BTBT film on the ZnPcPS$_4$/pyPMMA surface appeared to be influenced by the underlying polymer, as shown in Fig. 5(c). The surface morphology of C8-BTBT on the ZnPcPS$_4$ or pyPMMA homopolymers showed islands with a smooth top surface on a continuous layer, which appeared to follow the Stranski–Krastanov growth modes. The cross-sectional profiles of C8-BTBT on ZnPcPS$_4$ revealed that the step height of the islands was approximately 2.9 nm in the top layer and 2.6 nm on the second layer, with an underlying layer approximately 10 nm below (Fig. 5(c), middle). The long axis of C8-BTBT was approximately 3 nm,[46] suggesting that the molecule was aligned in a standing-up orientation normal to the substrate.[47] Meanwhile, the surface morphology of C8-BTBT on ZnPcPS$_4$/pyPMMA showed a similar layer and islands, but a relatively rough surface (Fig. 5(c), left). This indicates that the crystal growth of C8-BTBT occurs similarly to the flat PS and PMMA surfaces, but it is in accordance with the initial surface roughness of the phase-separated morphology (Fig. 5(d)). Indeed, the out-of-plane X-ray diffraction (XRD) profile of C8-BTBT on the blend or homopolymer showed almost the same patterns as those of the crystalline structures (Fig. S5, ESI†). The sharp peak at 2θ = 3.1°, originating from the (001) Bragg reflection, was estimated to have a d-spacing of 2.8 nm. Taken together with the AFM results, the C8-BTBT films formed highly ordered layer-by-layer phases, even on the phase-separated surface of ZnPcPS$_4$/pyPMMA, resulting in a comparable charge carrier mobility in OFET devices.

In the transfer curve of the memory devices embedded with ZnPc-containing polymers, a clear hysteresis was observed between forward and backward sweeps for V_g between +5 and −50 V at a fixed drain voltage (V_d) of −50 V (Fig. 5(b), left and middle). This result indicated that the holes accumulated in C8-BTBT were trapped in the memory layer while sweeping to a negative V_g. In contrast, no significant hysteresis was observed in devices with pyPMMA (Fig. 5(b), right). It should also be noted here that the charge carrier mobility values of the OFET devices with ZnPc-containing polymer layers were lower than those with pyPMMA. Since the crystal structure of C8-BTBT on ZnPcPS$_4$ or pyPMMA did not show clear differences in the AFM images, this discrepancy was probably due to charge trapping during sweeping, which could prevent efficient charge migra-tion in the organic semiconductor.[35] The magnitude of the hysteresis was maximal for the ZnPcPS$_4$-embedded memory device, which was approximately twice as large as that of the ZnPcPS$_4$/pyPMMA-embedded device. This result was reason-able because the concentration of ZnPc, i.e., the density of
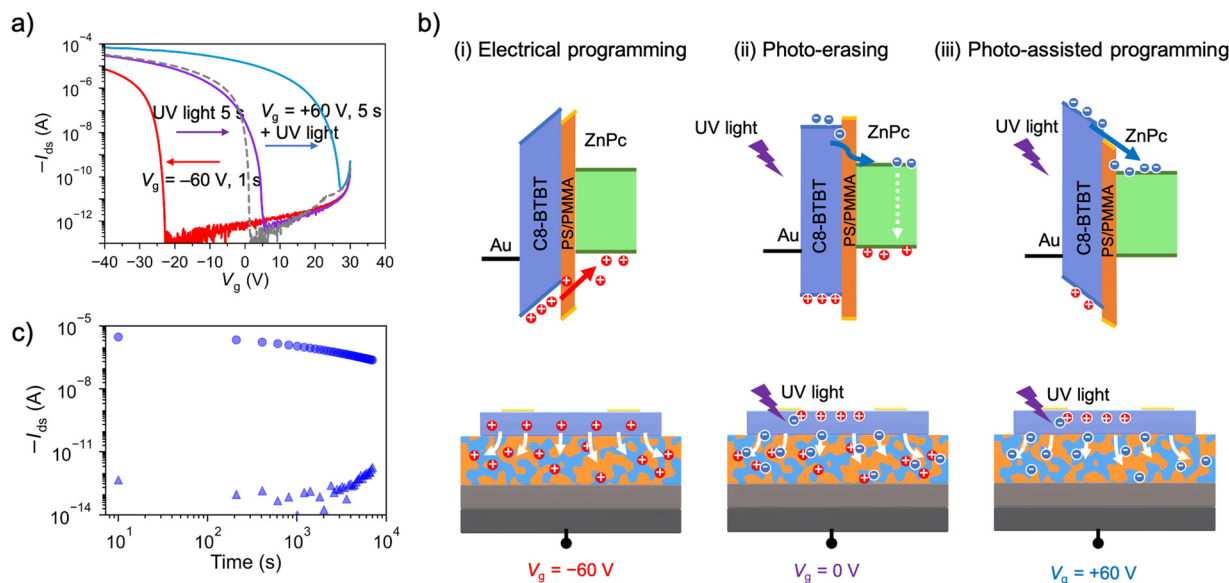
Fig. 6 (a) Transfer characteristics of the OFET memory device with a polymer layer of ZnPcPS$_4$/pyPMMA at V_d = −50 V. (b) Schematics and energy-level alignments during the (i) electrical programming operation, (ii) UV-light-assisted erasing operation, and (iii) UV-light-assisted programming operation. (c) Retention time of the I_{ds} monitored at V_g = 0 V and V_d = −10 V after hole-trapping (triangle) and electron-trapping (circle).

the charge-trapping site, was reduced by approximately half in the supramolecular μ-star film.

To quantitatively evaluate the memory performance, programming/erasing operations of the OFET memory devices were conducted by applying a V_g pulse and light irradiation. When a negative gate bias was applied to the ZnPcPS$_4$/pyPMMA-embedded OFET memory (V_g = −60 V for 1 s), the transfer curve shifted toward the negative direction (Fig. 6(a), red line). This process is referred to as programming (hole-trapping), in which the holes accumulated in the C8-BTBT semiconductor layer are transferred to and stored in the memory layer. The average shift of V_{th} ($\Delta V_{th(+)}$) was 25.4 V for the ZnPcPS$_4$/pyPMMA-embedded device and 31.5 V for the ZnPcPS$_4$-embedded device (Fig. S6, ESI†). The OFET memory with the pyPMMA layer showed a small shift of 5.3 V, confirming that significant charge trapping occurred owing to the presence of the ZnPc core (Fig. S7, ESI†). Interestingly, the erasing process was accomplished by UV light irradiation. When the OFET memory device was exposed to UV light (250–380 nm) with an intensity of 2.5 mW cm^{-2} for 5 s after the programming process, the transfer curve shifted back to the initial position (Fig. 6(a), purple line). This process is referred to as photo-erasing. By irradiating the device with UV light, a significant number of excitons (electron–hole pairs) can be generated on the semiconducting layer because C8-BTBT exhibits strong absorption in the UV region of the spectrum (Fig. S8, ESI†). Some electrons might effectively neutralize the trapped holes at the interface between the C8-BTBT layer and the underlying memory layer, achieving an erasing process in the absence of an electric field.[26,48] Another possible mechanism of photo-erasing is the annihilation of the trapped charges by excitons induced in the memory layer.[49,50] However, we found that photo-erasing could be completed by LED light irradiation

at 365 nm (Fig. S9a, ESI†), while 730 nm LED light irradiation, corresponding to the absorption of ZnPc, cannot complete this process (Fig. S9b, ESI†). Thus, charge annihilation may be primarily due to the excitons of C8-BTBT, as previously mentioned. Furthermore, when V_g = +60 V was applied for 5 s under UV irradiation, the transfer curve shifted in the positive direction as +21.9 V (Fig. 6(a), blue line). This process is referred to as photo-assisted programming (electron trapping). In this process, the photogenerated excitons were separated by an external electric field and some electrons were trapped in the underlying polymer layer. This resulted in a positive shift in V_{th}, eventually giving OFET memory devices a large memory window with ambipolar charge-trapping behavior. This photo-assisted programming process was not achieved by the LED light irradiation at 730 nm (Fig. S9b, ESI†). This indicates that excitons generated within the semiconductor triggered the memory programming. The proposed mechanisms of hole trapping, photo-erasing, and photo-assisted electron trapping are illustrated in Fig. 6(b). The positive V_{th} shift of the ZnPcPS$_4$/pyPMMA-embedded OFET memory device was larger than that of the ZnPcPS$_4$-embedded device. This result suggested that electrons were trapped not only in the ZnPc core but also in the polymer chains and/or interfaces. A similar trend was observed in the OFET memory with a memory layer of phase-separated block copolymer, where charge trapping occurred in the interfaces between the polymer domains.[21] Phase separation of the supramolecular μ-star might be favorable for electron trapping, resulting in a comparable memory window of approximately 47.0 V for all operations (Fig. S6, ESI†).

The conditions of the photo-assisted programming were also optimized by varying the applied V_g (Fig. S10a, ESI†). When the applied V_g was gradually increased from 0 to +60 V under light irradiation for 5 s, the memory window saturated at

This journal is © The Royal Society of Chemistry 2024

J. Mater. Chem. C, 2024, **12**, 9642–9651 | **9647**

V_g = +40 V, indicating that the applied voltage could be reduced by light irradiation. This result also suggested that the drain current can be controlled by applying voltage and/or light, thereby exhibiting potential applications in multilevel data storage (Fig. S10b, ESI†).

The retention time of the OFET memory device after the programming process was evaluated to demonstrate its reliability. As shown in Fig. 6(c), the drain current was monitored at V_g = 0 V under V_d = −10 V after applying V_g = −60 V for 1 s (OFF state) or V_g = +60 V for 5 s under UV light irradiation (ON state). These correspond to hole-trapped and electron-trapped states in OFET memory, respectively. The on/off current ratio remained at 10^5 after 3 h for the ZnPcPS$_4$/pyPMMA-embedded OFET memory device, indicating the superior charge retention capability of the polymer layer. Notably, ZnPcPS$_4$/pyPMMA showed a longer electron-trapping retention time than the ZnPcPS$_4$ and pyPMMA layers (Fig. S11, ESI†). Considering its large memory window and long charge-retention capability, the phase-separated morphology of ZnPcPS$_4$/pyPMMA was assumed to provide efficient charge trapping and suppress charge leakage. Therefore, the charge-trapping behaviors of the polymer films were investigated.

Charge-trapping properties in polymer memory layers

Charge injection, retention, and diffusion processes in the polymer films were studied using KPFM. The KPFM technique has been widely used to profile the localized electrical properties of films used in electronic devices because it can simultaneously obtain a high-resolution morphology and surface potential.[51,52] This technique allows the evaluation of the electrical potential difference,[53,54] charge transport and spatial distribution in the semiconductor channel,[55–57] work function for nanostructures,[58] and charge-trapping and diffusion properties in the dielectric layer.[59–61]

Three types of polymer films, ZnPcPS$_4$, ZnPcPS$_4$/pyPMMA, and pyPMMA, were prepared by spin-coating toluene solutions onto a highly doped n-type silicon wafer with a 300 nm SiO$_2$ layer. Charges were injected into the polymer film by contact with a conductive tip on the polymer surface with an applied voltage bias (V_{tip}), while the substrate was ground (Fig. 7(a)). As shown in Fig. 7(b), after injecting a positive bias (V_{tip} = +10 V)

for 30 s onto the ZnPcPS$_4$/pyPMMA film, a spot with a relatively positive potential was observed by scanning the surface potential using KPFM. This result indicates that the strong electric field between the tip and polymer surface extracts electrons by tunneling, inducing holes at the specific injection point. In contrast, electron injection was achieved by applying a negative bias of V_{tip} = −10 V for 30 s by the contact mode in KPFM. Localized charges were visualized by measuring the surface potential; a relatively negative spot was observed in a specific area of the injection point. The line profiles of the potential peaks after injecting holes or electrons into the ZnPcPS$_4$/pyPMMA film are plotted in Fig. 7(c), where the maximum potential peak decreased very slowly *via* charge diffusion. Note that the first point of the peak potential was approximately 10 min after charge injection owing to the AFM scanning experimental conditions. The peak potential at 10 min after applying a positive bias was 0.62 V and decreased to 0.32 V after 2 h, while the peak potential after a negative bias was −0.51 V at 10 min and remained at −0.32 V after 2.4 h.

To further investigate the charge retention and diffusion behavior of the polymer film, charge injection experiments were performed on other polymer thin films of ZnPcPS$_4$ and pyPMMA (Fig. S12, ESI†). The peak potential after the same injection experiments of positive charge was 0.62 V for ZnPcPS$_4$, which is a similar value to that of the ZnPcPS$_4$/pyPMMA film. Meanwhile, the pyPMMA film exhibited the peak potential at 0.42 V after charge injection. The higher peak potentials of the ZnPc-containing polymers indicate the efficient charge-trapping capability of the ZnPc cores in the polymer matrix. After applying a negative V_{tip}, the negative peak potentials were nearly identical across polymers, approximately 0.5 V. Subsequently, the peak potential maps were continuously analyzed every 8 min after injecting charges (hole or electron) into each polymer and the maximum peak potential was plotted over time. The time dependence of the peak potential of the polymer films is shown in Fig. 7(d), representing decay in the number of trapped charges in the polymer films. The plotted potential peak fits well with the exponential curve according to the following equation:

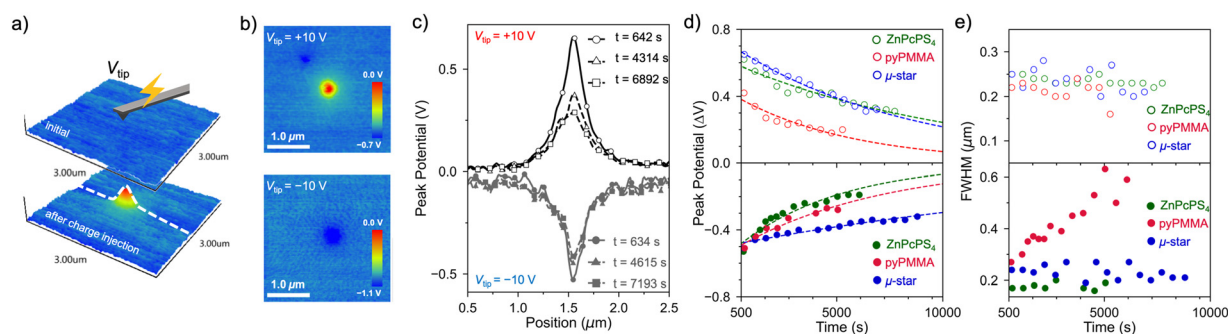$$Q(t) = Q_0 \exp\left(-\frac{t}{\tau}\right) \quad (4)$$

Fig. 7 (a) Schematics of charge-injection experiments using KPFM. (b) Surface potential images of the ZnPcPS$_4$/pyPMMA film after applying V_{tip} = +10 V (top) and −10 V (bottom). (c) Peak potential change after the charge injection. (d) Decays and exponential curve fittings of the peak potentials with time after charge injection into different polymers. (e) Evolution of the full width at half-maximum (FWHM) of potential curves with time for each polymer.

where Q_0 is the initial charge, t is the time after charge injection, and τ is the characteristic decay time, which is equal to the time to reach approximately 37% of the initial decay. The characteristic decay time of holes (τ_h) was approximately 1.1×10^4 s for the ZnPcPS$_4$ film and 8.5×10^3 s for ZnPcPS$_4$/pyPMMA, relatively longer than the 5.5×10^3 s for the pyPMMA film. This confirmed that the ZnPc-containing polymers have superior hole capture and retention capabilities. The dielectric PS arms effectively confined positive charges to the ZnPc core, resulting in localized areas of high charge density. More interestingly, the supramolecular μ-star film also showed an excellent retention capability of electrons. The decay time of electron (τ_e) trapping in the ZnPcPS$_4$/pyPMMA film was 2.0×10^4 s. The retention time was much shorter in ZnPcPS$_4$ (6.9×10^3 s) and pyPMMA (4.8×10^3 s). This result was consistent with the retention characteristics of electron-trapped states in the OFET memory device (Fig. S11, ESI†). Furthermore, the evolution of the full width at half-maximum (FWHM) of the potential curve with time was analyzed to investigate the charge diffusion properties in the polymer film (Fig. 7(e)). The potential spot size derived from the trapped hole was nearly constant for all the polymer films, indicating that the trapped holes in polymer dielectrics did not show lateral charge diffusion through the polymer matrix during the charge decay. Meanwhile, a rapid increase in spot size was monitored after injecting a negative voltage bias into the pyPMMA film. This electron diffusion feature was not observed in the case of the ZnPcPS$_4$/pyPMMA film. The phase separation between the PS and PMMA domains might inhibit the lateral diffusion of electrons. The ZnPcPS$_4$/pyPMMA film originally showed a different surface potential of approximately 0.1 V (Fig. S13, ESI†). This barrier might inhibit uniform potential diffusion throughout the polymer film. As a result, it was found that the ZnPcPS$_4$/pyPMMA film can stably store both electrons and holes, making it useful as a memory layer in OFET devices.

Conclusion

We investigated the effect of the film morphology of charge-trapping polymeric materials on the OFET memory devices using the supramolecular μ-star. The mixtures of ZnPcPS$_4$ and pyridine-terminated polymers (pyPMMA, pyPVAc, pyPVK) formed a supramolecular μ-star, and their spin-coated films exhibited unique microphase separation with smooth film surfaces due to the non-covalent interaction between polymers. The OFET memory device was fabricated using a ZnPcPS$_4$/pyPMMA film as the charge-trapping layer and C8-BTBT as the organic semiconductor. By combining the electric and photo-assisted programming operations, the memory device exhibited ambipolar charge-trapping characteristics. The memory device trapped holes by applying a negative V_g bias, released trapped charges by photoirradiation with UV light, and further trapped electrons when UV light and a positive V_g bias were applied simultaneously. Consequently, the memory device showed a large memory window (~ 47 V), a high I_{on}/I_{off} memory ratio ($\sim 10^7$), and long-term charge retention ($> 10^4$ s). KPFM

studies of the polymer films revealed that the ZnPc-containing films had efficient hole-trapping and long retention ability, whereas the ZnPcPS$_4$/pyPMMA films also showed superior retention ability of electrons owing to the surface potential difference at the interfaces of nanostructures of supramolecular μ-stars. Our study suggests that a design strategy for nanostructured charge-trapping materials with functional aromatic molecules can improve the performance of photo-transistor memory.

Author contributions

Conflicts of interest

The authors declare no competing interests.

Acknowledgements

References

1 T. Sekitani, T. Yokota, U. Zschieschang, H. Klauk, S. Bauer, K. Takeuchi, M. Takamiya, T. Sakurai and T. Someya, *Science*, 2009, **326**, 1516–1519.

2 M. L. Hammock, A. Chortos, B. C. Tee, J. B. Tok and Z. Bao, *Adv. Mater.*, 2013, **25**, 5997–6038.

3 A. Yamamura, H. Matsui, M. Uno, N. Isahaya, Y. Tanaka, M. Kudo, M. Ito, C. Mitsui, T. Okamoto and J. Takeya, *Adv. Electron. Mater.*, 2017, **3**, 1600456.

4 J. Hoffman, X. Pan, J. W. Reiner, F. J. Walker, J. P. Han, C. H. Ahn and T. P. Ma, *Adv. Mater.*, 2010, **22**, 2957–2961.

5 R. C. Naber, K. Asadi, P. W. Blom, D. M. de Leeuw and B. de Boer, *Adv. Mater.*, 2010, **22**, 933–945.

6 J. Y. Park, D. H. Choe, D. H. Lee, G. T. Yu, K. Yang, S. H. Kim, G. H. Park, S. G. Nam, H. J. Lee, S. Jo, B. J. Kuh, D. Ha, Y. Kim, J. Heo and M. H. Park, *Adv. Mater.*, 2023, **35**, 2204904.

7 K. J. Baeg, Y. Y. Noh, J. Ghim, S. J. Kang, H. Lee and D. Y. Kim, *Adv. Mater.*, 2006, **18**, 3179–3183.

This journal is © The Royal Society of Chemistry 2024

J. Mater. Chem. C, 2024, **12**, 9642–9651 | **9649**

8 Y. H. Chou, H. C. Chang, C. L. Liu and W. C. Chen, *Polym. Chem.*, 2015, **6**, 341–352.

9 H. C. Chang, C. Lu, C. L. Liu and W. C. Chen, *Adv. Mater.*, 2015, **27**, 27–33.

10 C. C. Shih, Y. C. Chiu, W. Y. Lee, J. Y. Chen and W. C. Chen, *Adv. Funct. Mater.*, 2015, **25**, 1511–1519.

11 L. Van Tho, K. J. Baeg and Y. Y. Noh, *Nano Convergence*, 2016, **3**, 1–7.

12 J. S. Lee, Y. M. Kim, J. H. Kwon, H. Shin, B. H. Sohn and J. Lee, *Adv. Mater.*, 2009, **21**, 178–183.

13 C. C. Shih, W. Y. Lee and W. C. Chen, *Mater. Horiz.*, 2016, **3**, 294–308.

14 Y. L. Guo, C. A. Di, S. H. Ye, X. N. Sun, J. Zheng, Y. G. Wen, W. P. Wu, G. Yu and Y. Q. Liu, *Adv. Mater.*, 2009, **21**, 1954–1959.

15 J. S. Lee, Y. M. Kim, J. H. Kwon, J. S. Sim, H. Shin, B. H. Sohn and Q. X. Jia, *Adv. Mater.*, 2011, **23**, 2064–2068.

16 M. Kang, K. J. Baeg, D. Khim, Y. Y. Noh and D. Y. Kim, *Adv. Funct. Mater.*, 2013, **23**, 3503–3512.

17 Y. Park, K. J. Baeg and C. Kim, *ACS Appl. Mater. Interfaces*, 2019, **11**, 8327–8336.

18 T. Xu, S. X. Guo, W. H. Qi, S. Z. Li, M. L. Xu and W. Wang, *ACS Appl. Mater. Interfaces*, 2020, **12**, 21952–21960.

19 H. Y. Chi, H. W. Hsu, S. H. Tung and C. L. Liu, *ACS Appl. Mater. Interfaces*, 2015, **7**, 5663–5673.

20 L. C. Hsu, T. Isono, Y. C. Lin, S. Kobayashi, Y. C. Chiang, D. H. Jiang, C. C. Hung, E. Ercan, W. C. Yang, H. C. Hsieh, K. Tajima, T. Satoh and W. C. Chen, *ACS Appl. Mater. Interfaces*, 2021, **13**, 2932–2943.

21 Y. C. Chen, Y. C. Lin, H. C. Hsieh, L. C. Hsu, W. C. Yang, T. Isono, T. Satoh and W. C. Chen, *J. Mater. Chem. C*, 2021, **9**, 1259–1268.

22 C. F. Lin, Y. C. Lin, W. C. Yang, L. C. Hsu, E. Ercan, C. C. Hung, Y. Y. Yu and W. C. Chen, *Adv. Electron. Mater.*, 2021, **7**, 2100655.

23 W. L. Leong, P. S. Lee, A. Lohani, Y. M. Lam, T. Chen, S. Zhang, A. Dodabalapur and S. G. Mhaisalkar, *Adv. Mater.*, 2008, **20**, 2325–2331.

24 Y. C. Chiu, I. Otsuka, S. Halila, R. Borsali and W. C. Chen, *Adv. Funct. Mater.*, 2014, **24**, 4240–4249.

25 Y. F. Yang, Y. C. Lin, E. Ercan, Y. C. Chiang, B. H. Lin and W. C. Chen, *Macromolecules*, 2022, **55**, 8262–8272.

26 M. D. Yi, M. Xie, Y. Q. Shao, W. Li, H. F. Ling, L. H. Xie, T. Yang, Q. L. Fan, J. L. Zhu and W. Huang, *J. Mater. Chem. C*, 2015, **3**, 5220–5225.

27 T. Y. Huang, C. H. Chen, C. C. Lin, Y. J. Lee, C. L. Liu and G. S. Liou, *J. Mater. Chem. C*, 2019, **7**, 11014–11021.

28 Y. C. Chiang, C. C. Hung, Y. C. Lin, Y. C. Chiu, T. Isono, T. Satoh and W. C. Chen, *Adv. Mater.*, 2020, **32**, 2002638.

29 Y. F. Yang, Y. C. Chiang, Y. C. Lin, G. S. Li, C. C. Hung and W. C. Chen, *Adv. Funct. Mater.*, 2021, **31**, 2102174.

30 Y. C. Lin, W. C. Yang, Y. C. Chiang and W. C. Chen, *Small Sci.*, 2022, **2**, 2100109.

31 W. C. Yang, Y. C. Lin, S. Inagaki, H. Shimizu, E. Ercan, L. C. Hsu, C. C. Chueh, T. Higashihara and W. C. Chen, *Adv. Sci.*, 2022, **9**, 2105190.

32 T. F. Yu, H. Y. Chen, M. Y. Liao, H. C. Tien, T. T. Chang, C. C. Chueh and W. Y. Lee, *ACS Appl. Mater. Interfaces*, 2020, **12**, 33968–33978.

33 Y. T. Yang, H. C. Tien, C. C. Chueh and W. Y. Lee, *Mater. Chem. Phys.*, 2022, **287**, 126263.

34 J. Aimi, C. T. Lo, H. C. Wu, C. F. Huang, T. Nakanishi, M. Takeuchi and W. C. Chen, *Adv. Electron. Mater.*, 2016, **2**, 1500300.

35 J. Aimi, P. H. Wang, C. C. Shih, C. F. Huang, T. Nakanishi, M. Takeuchi, H. Y. Hsueh and W. C. Chen, *J. Mater. Chem. C*, 2018, **6**, 2724–2732.

36 J. Aimi, T. Yasuda, C.-F. Huang, M. Yoshio and W.-C. Chen, *Mater. Adv.*, 2022, **3**, 3128–3134.

37 D. Panigrahi, R. Hayakawa, X. H. Zhong, J. Aimi and Y. Wakayama, *Nano Lett.*, 2023, **23**, 319–325.

38 R. Hayakawa, K. Takahashi, X. Zhong, K. Honma, D. Panigrahi, J. Aimi, K. Kanai and Y. Wakayama, *Nano Lett.*, 2023, **23**, 8339–8347.

39 X. H. Zhong, A. Nagai, M. Takeuchi and J. Aimi, *Macromol. Rapid Commun.*, 2023, **44**, 2200666.

40 A. E. Levi, L. B. Fu, J. Lequieu, J. D. Home, J. Blankenship, S. Mukherjee, T. Q. Zhang, G. H. Fredrickson, W. R. Gutekunst and C. M. Bates, *Macromolecules*, 2020, **53**, 702–710.

41 T. Y. Lin, C. W. Tu, J. Aimi, Y. W. Huang, T. Jamnongkan, H. Y. Hsueh, K. Y. A. Lin and C. F. Huang, *Nanomaterials*, 2021, **11**, 2392.

42 V. Sathesh, J. K. Chen, C. J. Chang, J. Aimi, Z. C. Chen, Y. C. Hsu, Y. S. Huang and C. F. Huang, *Polymers*, 2018, **10**, 858.

43 F. Bates, *Science*, 1991, **251**, 898–905.

44 S. Walheim, M. Böltau, J. Mlyneck, G. Krausch and U. Steiner, *Macromolecules*, 1997, **30**, 4995–5003.

45 H. Ebata, T. Izawa, E. Miyazaki, K. Takimiya, M. Ikeda, H. Kuwabara and T. Yui, *J. Am. Chem. Soc.*, 2007, **129**, 15732–15733.

46 C. Grigoriadis, C. Niebel, C. Ruzié, Y. H. Geerts and G. Floudas, *J. Phys. Chem. B*, 2014, **118**, 1443–1451.

47 S. T. Wang, D. M. Niu, L. Lyu, Y. B. Huang, X. H. Wei, C. Wang, H. P. Xie and Y. L. Gao, *Appl. Surf. Sci.*, 2017, **416**, 696–703.

48 C. Sun, Z. Lin, W. Xu, L. Xie, H. Ling, M. Chen, J. Wang, Y. Wei, M. Yi and W. Huang, *J. Phys. Chem. C*, 2015, **119**, 18014–18021.

49 Y. J. Jeong, D. J. Yun, S. H. Kim, J. Jang and C. E. Park, *ACS Appl. Mater. Interfaces*, 2017, **9**, 11759–11769.

50 M. N. Chen, S. W. Chang, S. P. Prakoso, Y. T. Li, K. L. Chen and Y. C. Chiu, *ACS Appl. Mater. Interfaces*, 2021, **13**, 44656–44662.

51 V. Palermo, M. Palma and P. Samorì, *Adv. Mater.*, 2006, **18**, 145–164.

52 C. Musumeci, A. Liscio, V. Palermo and P. Samorì, *Mater. Today*, 2014, **17**, 504–517.

53 A. Liscio, V. Palermo and P. Samorì, *Adv. Funct. Mater.*, 2008, **18**, 907–914.

54 L. Gross, F. Mohn, N. Moll, P. Liljeroth, J. Repp, F. J. Giessibl and G. Meyer, *Science*, 2009, **324**, 1428–1431.

9650 | *J. Mater. Chem. C*, 2024, **12**, 9642–9651

This journal is © The Royal Society of Chemistry 2024

55 J. A. Nichols, D. J. Gundlach and T. N. Jackson, *Appl. Phys. Lett.*, 2003, **83**, 2366–2368.

56 Y. Yamagishi, K. Noda, K. Kobayashi and H. Yamada, *J. Phys. Chem. C*, 2015, **119**, 3006–3011.

57 R. Hayakawa, S. Takeiri, Y. Yamada and Y. Wakayama, *Adv. Mater. Interfaces*, 2023, **10**, 2201857.

58 G. H. Enevoldsen, T. Glatzel, M. C. Christensen, J. V. Lauritsen and F. Besenbacher, *Phys. Rev. Lett.*, 2008, **100**, 236104.

59 S. G. J. Mathijssen, M. Kemerink, A. Sharma, M. Coelle, P. A. Bobbert, R. A. J. Janssen and D. M. de Leeuw, *Adv. Mater.*, 2008, **20**, 975–979.

60 S. Paydavosi, K. E. Aidala, P. R. Brown, P. Hashemi, G. J. Supran, T. P. Osedach, J. L. Hoyt and V. Bulovic, *Nano Lett.*, 2012, **12**, 1260–1264.

61 J. Wang, X. Wang, W. J. Xu, L. H. Xie, Y. Y. Liu, M. D. Yi and W. Huang, *Phys. Chem. Chem. Phys.*, 2016, **18**, 9412–9418.

This journal is © The Royal Society of Chemistry 2024

J. Mater. Chem. C, 2024, **12**, 9642–9651 | **9651**